

Super-Resolved Canopy Height Mapping from Sentinel-2 Time Series Using LiDAR HD Reference Data across Metropolitan France

Ekaterina Kalinicheva^a, Florian Helen^b, Stéphane Mermoz^b, Florian Mouret^a, Milena Planells^a

^a*CESBIO, 18 avenue Édouard Belin, Toulouse, 31401, France*

^b*GlobEO, Avenue Saint-Éxupéry, Toulouse, 31400, France*

Abstract

Fine-scale forest monitoring is essential for understanding canopy structure and its dynamics, which are key indicators of carbon stocks, biodiversity, and forest health. Deep learning is particularly effective for this task, as it integrates spectral, temporal, and spatial signals that jointly reflect the canopy structure. To address this need, we introduce THREASURE-Net, a novel end-to-end framework for Tree Height Regression And Super-Resolution. The model is trained on Sentinel-2 time series using reference height metrics derived from LiDAR HD data at multiple spatial resolutions over Metropolitan France to produce annual height maps. We evaluate three model variants, producing tree-height predictions at 2.5 m, 5 m, and 10 m resolution. THREASURE-Net does not rely on any pretrained model nor on reference very high resolution optical imagery to train its super-resolution module; instead, it learns solely from LiDAR-derived height information. Our approach outperforms existing state-of-the-art methods based on Sentinel data and is competitive with methods based on very high resolution imagery. It can be deployed to generate high-precision annual canopy-height maps, achieving mean absolute errors of 2.62 m, 2.72 m, and 2.88 m at 2.5 m, 5 m, and 10 m resolution, respectively. These results highlight the potential of THREASURE-Net for scalable and cost-effective structural monitoring of temperate forests using only freely available satellite data. The source code for THREASURE-Net is available at: <https://github.com/Global-Earth-Observation/threasure-net>.

Keywords: forest canopy height regression, super-resolution, Sentinel-2 time series, LiDAR HD, temporal transformer

1. Introduction

Nowadays, forest monitoring is essential to capture the spatial heterogeneity in canopy structure and dynamics that drives carbon storage variability, species diversity, and early detection of forest health decline in the context of climate change (FAO, 2025). However, many forest processes – such as selective logging, canopy degradation, regeneration, or subtle structural changes – occur at fine spatial scales that cannot be captured by coarse imagery (Cally et al., 2025; Duncanson et al., 2025). Indeed, some vegetation monitoring tasks require finer spatial detail, especially in forests, where small-scale dynamics can indicate the early stages of irreversible change (Mitchell et al., 2017).

Canopy height prediction is a key component of forest monitoring, as it provides insights into stand structure, biomass, regeneration dynamics, and disturbance impacts (Lang et al., 2023). Although this task is not new (Simard et al., 2011), the methods and spatial resolutions involved have evolved substantially over time. While early approaches relied on coarse to medium resolution imagery combined with traditional machine learning models such as Random Forests (Morin et al., 2023; Ahmed et al., 2015; Wang et al., 2016), more recent works have shown that deep learning methods can predict canopy structure at much finer spatial resolutions, substantially improving height prediction accuracy (Fogel et al., 2025).

Moreover, forest dynamics are increasingly studied in their

temporal context (Bugmann and Seidl, 2022), as analyzing changes over time is essential for understanding regrowth patterns, disturbance impacts, and long-term structural evolution. However, detecting small, subtle temporal changes remains particularly challenging, even though such early signals often mark the onset of potentially irreversible processes Liu et al. (2019). Therefore, enhancing canopy height prediction at fine spatial resolution and at frequent intervals remains an open challenge, especially in rapidly changing forest ecosystems where small-scale dynamics carry important ecological significance.

To monitor canopy evolution across large territories over time, researchers increasingly rely on satellite imagery as a practical source of information (Besic et al., 2025). While low- to medium-resolution data are freely available and provide broad spatial and temporal coverage, acquiring high-resolution reference data remains expensive and is often limited in availability (Fassnacht et al., 2023). Therefore, training models directly on very high-resolution (VHR) imagery at regional or national scales is often impractical and costly.

In this context, two central research questions remain open: how can prediction accuracy be further improved, and how can very high-resolution canopy height estimates be produced while keeping data acquisition costs low. To address these questions, we focus in this work on improving tree height prediction while simultaneously increasing the output resolution using only freely available remote sensing data.

In recent years, satellite data from missions such as Sentinel-

1 and Sentinel-2 have been widely used to monitor and predict various forest structural and biophysical characteristics over time (Santoro et al., 2024; Mermoz et al., 2024). While Sentinel-2 offers dense time series capturing seasonal variations, most approaches focus on summarizing these observations to derive annual estimates of forest structure (Lang et al., 2023).

Nevertheless, manual annotation of forest stands at large scales to obtain reference data is impractical and often impossible. As a result, it has become common practice to use LiDAR (Light Detection and Ranging) data – whether airborne or satellite-based – to derive reference data. Among the most widely used sources are GEDI (Dubayah et al., 2020) – a space-borne LiDAR mission providing discrete vertical profiles at 25-m resolution – and various airborne LiDAR campaigns.

Today, airborne LiDAR data remains the most accurate and comprehensive source of information for forest structure monitoring and analysis (Coops et al., 2021). It provides detailed 3D point clouds whose spatial resolution – directly linked to point density – allows the precise characterization of forest vertical and horizontal structure. Therefore, various metrics derived from LiDAR data in raster shape at different resolutions often serve as reference data to train various machine learning models based on satellite imagery (Coops et al., 2021). In France, the LiDAR HD¹ national campaign aims to cover the entire metropolitan territory with a minimum density of 10 pulses per m², which constitutes a key reference dataset for forest structural studies. However, despite its extensive coverage of French territory, each area is typically observed only once, which prevents any temporal analysis using LiDAR HD data alone. Hence, the high point density of the LiDAR HD data enables the extraction of forest metrics at fine spatial resolutions, providing valuable reference datasets for VHR tree height prediction.

Today, many researchers across different domains seek to bridge the gap between commonly available medium- and low-resolution data and the rare VHR data necessary for accurate modeling and analysis (Lepcha et al., 2023). Recent advances in deep learning and image processing have made it possible to enhance the spatial resolution of input data, opening new opportunities for both image and video analysis – from capturing finer details to enabling high-quality restoration (Wang et al., 2021).

This progress has also strongly influenced the field of remote sensing, where improving the spatial resolution of satellite imagery has become a central goal (Wang et al., 2022a; Vu-Duc et al., 2025). While medium resolution satellite imagery, such as Sentinel-2 data, is freely available and provides global Earth coverage with 5-days revisit period (Drusch et al., 2012), VHR images are typically restricted for commercial use or offer limited spatial and/or temporal coverage. Therefore, many recent algorithms aim to transfer these high resolution (HR) features to low resolution (LR) imagery to overcome this limitation (Wang et al., 2022b).

While most of the studies focus on a super-resolution (SR) task alone (Salgueiro Romero et al., 2022; Liu et al., 2025; Michel et al., 2025; Müller et al., 2020), some studies integrate SR with a real-life prediction task to exploit rich spatial features of recovered high resolution details. Most of those works focus on semantic segmentation since the fine-texture spatial details are particularly valuable for object delineation.

For instance, Lei et al. (2019) use a dataset of small RGB image patches depicting airplanes, ships, and oil tanks. Low-resolution inputs are generated by downsampling the original high-resolution patches by a factor of four, and a joint super-resolution and segmentation network is then trained. In Abadal et al. (2021), the authors propose a Dual Network for Super-Resolution and Semantic Segmentation with a feature-affinity loss. In their approach, Sentinel-2 imagery is first downsampled to 20 m to create LR–HR pairs, and the network is trained to perform both SR and land-cover semantic segmentation. Deng et al. (2025) introduce the ISASeg model for semantic segmentation of impervious surface areas at 1 m resolution, using Jilin-1 VHR imagery as the SR supervision dataset. Finally, Cao and Weng (2024) investigate a different prediction task – building height regression at 2.5 m – where Sentinel-2 images serve as input and Google Earth imagery provides the target data.

In this context, downsampling high-resolution optical images to create training pairs is a common practice, but it introduces unrealistic low-resolution inputs and removes important low-feature information. In contrast, obtaining genuine high-resolution datasets is often prohibitively costly, limiting the availability of accurate ground-truth data.

As shown, state-of-the-art methods focus mostly on joint Single Image Super Resolution (SISR) analysis since their prediction tasks itself do not benefit from multi-temporal data. However, for certain applications, in particular, for vegetation analysis, capturing phenological variation across time is crucial for accurate prediction (Pelletier et al., 2018).

In contrast, Multi-Image Super-Resolution (MISR) techniques aim to jointly exploit multiple observations of the same area to reconstruct a higher resolution image. These methods have demonstrated significant gains in domains such as video restoration or change detection, yet they are rarely explored in the context of Earth Observation time series.

While we have not found any works performing simultaneously MISR and an associated downstream task, some works performing MISR alone can be cited. These approaches can be broadly categorized into: (i) temporal-transformer models that learn a shared temporal representation before upsampling (Okabayashi et al., 2024), (ii) diffusion-based models that reconstruct high-resolution outputs by iteratively denoising samples conditioned on the low-resolution inputs (Luo et al., 2024), and (iii) recursive fusion models (Deudon et al., 2020), that progressively merge the low-resolution observations.

Today several SISR models (Michel et al., 2025; Cresson, 2022) can be exploited to super-resolve Sentinel-2 satellite image time series (SITS). Consecutively, this new VHR SITS can then be directly used as an input for a prediction algorithm, the computational cost of processing a super-resolved series is drastically higher than the low resolution ones. Moreover, er-

¹<https://geoservices.ign.fr/lidarhd>

rors in image calibration and co-registration within a time series can introduce significant misalignments with the reference data, leading to substantial inconsistencies in the super-resolved input time series.

Motivated by these findings, we propose a novel end-to-end framework for forest canopy height regression from Sentinel-2 time series while simultaneously performing super-resolution. Our model, named THREASURE-Net (Tree Height REgression And SUper REsolution), allows us to generate tree height maps at 2.5, 5 and 10 m spatial resolutions. Our algorithm performance outperforms state-of-the-art methods based on Sentinel data and is competitive with methods based on very high resolution imagery, and can be exploited to produce high-precision annual height maps.

Our main contributions can be summarized as follows:

- We propose a fully end-to-end model that does not rely on any pretrained super-resolution networks or any VHR reference optical image data.
- THREASURE-Net trained solely on Sentinel-2 data achieves an accuracy comparable to models trained on VHR satellite data, while also providing coherent fine-scale spatial details that are not visible in predictions at the native resolution.
- During training, model predictions are conditioned by LiDAR’s acquisition date, explicitly accounting for the seasonal variability of reference data. Furthermore, the inference can be performed for any day of the year.
- The model is able to handle irregular Sentinel-2 time series acquired during the leaf-on season (from May to October of the same year) without explicitly requiring cloud-free observations.

2. Data

For model training and inference, we have prepared a training dataset spanning the entire area of metropolitan France, which corresponds to 80 Sentinel-2 tiles following the Military Grid Reference System (MGRS). Each tile is divided into $1 \times 1\text{km}$ LiDAR HD (national LiDAR campaign that aims to cover the whole french territory with density 10 pts/m^2) patches acquired over 2021-2024 years, resulting in 179945 patches for training, 19133 for validation, and 35639 for testing. We spatially and temporally match each LiDAR HD patch with Sentinel-2 images time series. The spatial distribution of the reference LiDAR patches is shown in Figure 1.

To build Sentinel-2 SITS, we choose images acquired from May to October, on the same year as the reference LiDAR HD patch. We filter out images with cloud coverage and missing data superior to 50% and 10%, respectively.

Sentinel-2 image time series correspond to the Level 2A product, processed from L1C by MAJA² algorithm developed

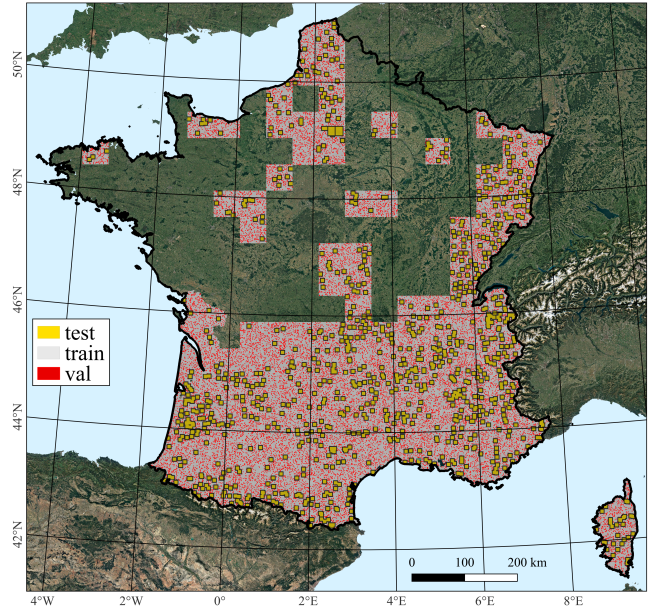


Figure 1: Distribution of train, test and validation patches. Buffers of 1 km are set around test patches to ensure reliable evaluation of model results.

by THEIA. We select 10 spectral bands (B02, B03, B04, B05, B06, B07, B08, B8A, B11, B12), Cloud Mask, as well as acquisition angles: Sun azimuth and zenith angles - θ_{S_a} and θ_{S_z} respectively, satellite mean view azimuth θ_{V_a} and zenith angles θ_{V_z} . All bands and angles are resampled at 10m. The acquisition angles are encoded using trigonometric transformations to respect angular periodicity:

$$[\cos(\theta_{S_z}), \cos(\theta_{S_a}), \sin(\theta_{S_a}), \cos(\theta_{V_z}), \cos(\theta_{V_a}), \sin(\theta_{V_a})].$$

Due to the coarse resolution of the available angle data (5 km pixel size), the angle values are extracted as vectors corresponding to the center of each patch.

The reference data are derived from LiDAR HD 3D point clouds and transformed to height rasters in a fully-automatic way: point cloud values are projected onto a regular pixel grid of chosen spatial resolution, from which the 95th percentile of elevation values is computed for every pixel. The LiDAR HD product is provided with point-wise classification into multiple land cover categories. Tree height values are only derived for pixels corresponding to vegetation higher than 1.5m, while the remaining pixels are set to zero. However, some tall vegetation crops, such as corn, may be classified as forest vegetation, introducing potential bias into model training, as crop vegetation does not follow the same structural or phenological characteristics as trees. To solve this issue, we apply a crop mask derived from Land Parcel Identification System (Le Registre Parcellaire Graphique (RPG)³. All vegetation within crop

²<https://www.cesbio.cnrs.fr/maja/>

³<https://artificialisation.developpement-durable.gouv.fr/bases donnees/registre-parcellaire-graphique>, the French national graphic crop register

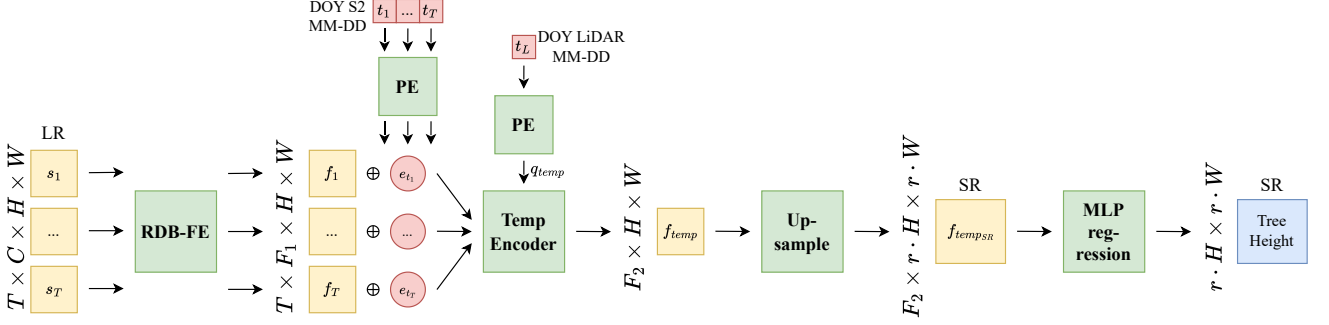


Figure 2: THREASURE-Net model architecture.

parcels with height below 5m is considered non-permanent, and its height values are excluded from the annotations.

3. Methodology

3.1. Model

In this work, we propose an end-to-end model, named THREASURE-Net, that performs super-resolution and regression tasks simultaneously. Given a Sentinel-2 SITS $s = [s_{t_1}, s_{t_2}, \dots, s_{t_T}] \in \mathbb{R}^{T \times C \times H \times W}$ acquired at dates $t = [t_1, t_2, \dots, t_T] \in \mathbb{R}^T$, the model aims to predict the tree height 95th percentile corresponding to the reference date t_L , producing an output of shape $f \cdot H \times f \cdot W$, where f denotes the SR factor. Note that for the sake of simplicity, we omit batch dimension in the model description.

THREASURE-Net model is composed of several blocks, as shown in Figure 2:

Spatio-spectral (SS) feature extraction module. First, we extracted features independently for each SITS image with Residual Dense Blocks-based Feature Extraction module (here referred to as RDB-FE). This produces a new feature time series $f = [f_{t_1}, f_{t_2}, \dots, f_{t_T}] \in \mathbb{R}^{T \times F_1 \times H \times W}$, where the new feature dimension F_1 is a hyperparameter.

The RDB-FE module is extracted from Residual Residual Dense network (RDN) (Zhang et al., 2018), which is mainly used for natural image SISR task and originally consists of four parts: shallow feature extraction net (SFENet), residual dense blocks (RDBs), dense feature fusion (DFF) and finally the up-sampling net (UPNet). Given the multi-temporal nature of our model, at this stage, we only deploy the feature extraction modules (SFENet, RDBs, and DFF). The up-sampling module is applied later to the temporally encoded features, rather than to each image individually.

While alternative architectures such as ResNet (He et al., 2015) or Residual-in-Residual Dense Blocks (RRDB) (Wang et al., 2018) could also be employed for feature extraction, we selected RDBs as a balanced choice. RDBs offer improved feature reuse compared to ResNet, thanks to dense connections that help capture fine-grained spatial details in Sentinel-2 imagery. At the same time, RDBs are significantly lighter than RRDBs, making them particularly well suited for our multi-temporal super-resolution task.

Temporal feature extraction block. To extract a unique set of temporal features for each Sentinel-2 series, we exploit the Lightweight Temporal Self-Attention mechanism proposed by Garnot and Landrieu (2020). The module captures dependencies across the multi-temporal Sentinel-2 time series and allows the network to dynamically weight the contribution of each timestamp, by using keys K , queries Q and values V to produce a self-attention mask. While K and V are directly derived from encoded features f and encoded temporal positions p of Sentinel-2, Q is a learnable parameter. For detailed explanation of Lightweight Temporal Transformer, the reader is invited to consult the original article. The simplified version of this algorithm can be summarized as follows (here we omit the explanation of the multi-head strategy):

Let $\mathbf{f} = [\mathbf{f}_1, \mathbf{f}_2, \dots, \mathbf{f}_T] \in \mathbb{R}^{T \times F_1}$ be the sequence of encoded S2 observations acquired at times $\{t_1, \dots, t_i, \dots, t_T\}$. Each timestamp is associated with a temporal encoding $\mathbf{p}_i \in \mathbb{R}^d$ obtained using a sinusoidal positional function:

$$\mathbf{p}_i^{(2k)} = \sin\left(\frac{t_i}{\tau^{2k/d}}\right), \quad \mathbf{p}_i^{(2k+1)} = \cos\left(\frac{t_i}{\tau^{2k/d}}\right), \quad (1)$$

where τ is a scaling constant and k indexes the embedding dimensions.

$$\tilde{\mathbf{f}}_i = \mathbf{f}_i + \mathbf{p}_{t_i}. \quad (2)$$

The attention mechanism computes keys and values as linear projections:

$$\mathbf{K} = \tilde{\mathbf{F}}W_K, \quad \mathbf{V} = \tilde{\mathbf{F}}W_V, \quad (3)$$

with learnable weights $W_K, W_V \in \mathbb{R}^{d \times d_a}$.

A single learnable query vector $\mathbf{q} \in \mathbb{R}^{d_a}$ is used to summarize the temporal sequence by computing attention weights:

The attention weights are then obtained as:

$$\alpha = \text{softmax}\left(\frac{\mathbf{K} \mathbf{q}_L^\top}{\sqrt{d_a}}\right),$$

giving the final aggregated temporal representation is:

$$\mathbf{f}_{temp} = \alpha^\top \mathbf{V}. \quad (4)$$

with final size $T \times F_2 \times H \times W$, where the new feature dimension F_2 is a hyperparameter.

However, since LiDAR HD reference data are acquired on different days of the year, the prediction quality may be affected by seasonal growth and on/off-leaf specificity of 3D LiDAR data. Therefore, we replace learnable queries from the original algorithm by temporal queries \mathbf{q}_{temp} that condition the predicted temporal features by LiDAR acquisition day, by projecting them onto a temporally-aware latent space.

$$\mathbf{q}_{temp} = W_Q \mathbf{e}_{t_L}, \quad (5)$$

where learnable weights $W_Q \in \mathbb{R}^{d \times d_a}$.

The LiDAR date t_L is encoded using the same sinusoidal positional encoding (eq. 1) as the Sentinel-2 acquisition dates t , ensuring that both modalities share a common temporal representation space. Finally, f_{temp} serves as the temporally fused feature used for downstream regression.

As described previously, we encode both the Sentinel-2 acquisition dates t and the reference LiDAR acquisition date t_L . The dates are expressed as day-of-year (DOY) values, $t = [t_1, \dots, t_i, \dots, t_T] \in \mathbb{R}^T$ and $t_L \in \mathbb{R}$, in “DD–MM” format, with the year omitted to ensure generalization across unseen years. Before applying the sinusoidal positional encoding, the DOY values are normalized as follows:

$$t_i = t_i - t_{\text{ref}, \text{S2}}, \quad \text{with } t_{\text{ref}, \text{S2}} = \text{January 1st.} \quad (6)$$

$$t_L = t_L - t_{\text{ref}, \text{L}}, \quad \text{with } t_{\text{ref}, \text{L}} = \text{July 1st.} \quad (7)$$

As shown in Equations 6 and 7, the resulting DOYs represent relative time offsets (in days) from the beginning and the middle of the year, respectively. This preprocessing highlights the seasonal relationship between the LiDAR reference date and the Sentinel-2 time series, allowing the model to better capture phenological phase alignment. During inference, predictions are by default conditioned on July 1st, whereas during training the DOY representation preserves temporal offsets around this date, enabling the model to encode whether an observation occurs earlier or later in the seasonal cycle.

Moreover, we use time series padding along the temporal dimension within each batch, which allows us to process SITS of various length.

Upsampling block. The upsampling step is applied after the temporal encoding rather than before, in order to reduce memory consumption—since a single shared temporally encoded feature map is upsampled instead of multiple individual ones—and to take advantage of the common temporal representation rather than processing separate temporal features independently.

The upsampling module employs a sub-pixel convolution (pixel shuffle) method (Shi et al., 2016), which reconstructs high-resolution outputs by rearranging low-resolution feature channels into spatial dimensions (see Figure 3). The SR is performed progressively by increasing the feature map resolution by a factor of 2 until the desired resolution is achieved. Therefore, the super-resolution hyperparameter r is constrained to be a power of 2. In each SR block with $r = 2$, the input feature map’s feature dimension F_2 is increased by factor

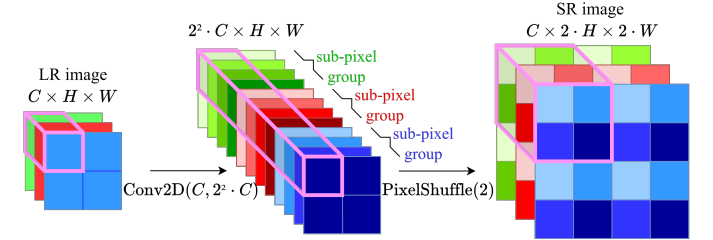


Figure 3: Sub-pixel convolution. Example of factor 2 upsampling. A LR image with C feature channels and $H \times W$ spatial dimensions is passed through 2D convolution layer to obtain $2^2 \cdot C$ feature channels where each group of 2^2 consecutive channels form a sub-pixel group that is reorganized by pixel shuffle operation to a SR image with C channels and $2 \cdot H \times 2 \cdot W$ spatial dimensions.

2^2 with a 2D convolution operation, then the resulted feature map is rearranged by a pixel shuffle operation, producing a new feature map of size $F_2 \times 2H \times 2W$: $\text{Conv2D}(F_2, 4 \cdot F_2) \rightarrow \text{PixelShuffle}(2)$. The sequence of those blocks is followed by another 2D convolution operation with ReLU activation, without changing the feature map size.

However, the sub-pixel convolutions are known to produce checkerboard artifacts (Aitken et al., 2017), due to random weight initialization across sub-pixel groups. To mitigate this issue, the weights are initialized following the approach presented by Aitken et al. (2017), where identical initialization is applied within each sub-pixel group to ensure smooth and artifact-free textures. A small amount of random noise is then added to break the symmetry and improve optimization dynamics.

Tree height regression. The final tree-height predictions are produced by a Multi-Layer Perceptron (MLP) that takes super-resolved features as input and outputs a regression map of tree heights at the selected resolution.

3.2. Loss functions

To optimize the model, the following loss functions are used: Mean Absolute Error (MAE) for tree height prediction, and Weighted Gradient Difference Loss (WGDL) to enhance the texture and edges of super-resolved features.

$$\mathcal{L}_{\text{total}} = \omega_{\text{height}} \cdot \mathcal{L}_{\text{height}} + \omega_{\text{wgdl}} \cdot \mathcal{L}_{\text{wgdl}} \quad (8)$$

Tree height regression Loss. As mentioned earlier, the MAE loss is employed for tree height prediction. However, we assume that most patches exhibit low variability in pixel values due to the homogeneous forest structure, which may lead to imbalance within a batch. To solve this issue, instead of directly averaging pixel-wise loss values across the batch, we first average them within each patch and then across patches in the batch as follows:

$$\mathcal{L}_{\text{batch}} = \frac{1}{B} \sum_{b=1}^B \left(\frac{1}{N_b} \sum_{i=1}^{N_b} \ell(p_{b,i}) \right) \quad (9)$$

where B is the batch size, N_b is the number of valid pixels within a patch and $\ell(p_{b,i})$ are pixel-wise loss values.

Gradient difference Loss. To improve the quality of the super-resolution, we employ the WGDL, a variant of Gradient Difference Loss (GDL) (Nie et al., 2018), which offers an effective balance between memory consumption and prediction accuracy. GDL loss is computed as L1 or L2 loss between the predicted and target image gradients for adjacent pixels in horizontal and vertical planes.

We define horizontal and vertical gradients ∇_x and ∇_y for predicted and reference images X and Y , respectively, as follows:

$$\begin{aligned}\nabla_x X_{i,j} &= X_{i,j} - X_{i,j-1}, & \nabla_y X_{i,j} &= X_{i,j} - X_{i-1,j}, \\ \nabla_x Y_{i,j} &= Y_{i,j} - Y_{i,j-1}, & \nabla_y Y_{i,j} &= Y_{i,j} - Y_{i-1,j}.\end{aligned}\quad (10)$$

where (i, j) are indexed pixel coordinates.

Then the GDL loss is computed as follows:

$$\begin{aligned}\mathcal{L}_{\text{GDL}}(X, Y) &= \left(\sum_{\substack{i=1 \\ j=1}}^{H,W} \left| |\nabla_x X_{i,j}| - |\nabla_x Y_{i,j}| \right|^\alpha \right. \\ &\quad \left. + \sum_{\substack{i=1 \\ j=1}}^{H,W} \left| |\nabla_y X_{i,j}| - |\nabla_y Y_{i,j}| \right|^\alpha \right) / 2,\end{aligned}\quad (11)$$

where α is the chosen loss function. In our work, L2-loss function is chosen. However, due to the homogeneous forest structure, the latter pixels will contribute more to the loss, while the textured/edge regions will be underrepresented. To address this issue, we propose the context-adapted pixel weighting strategy: the pixel weights are based on the target gradients normalized by the maximum gradient values $\max(|\nabla_x Y|)$ and $\max(|\nabla_y Y|)$ within each patch. Moreover, to prevent excluding homogeneous regions, we introduce the λ_{\min} regularization term, to ensure that the weights values are comprised in $[\lambda_{\min}, 1]$:

$$\begin{aligned}W_{\nabla_x}(i, j) &= \lambda_{\min} + (1 - \lambda_{\min}) \frac{|\nabla_x Y_{i,j}|}{\max(|\nabla_x Y|)}, \\ W_{\nabla_y}(i, j) &= \lambda_{\min} + (1 - \lambda_{\min}) \frac{|\nabla_y Y_{i,j}|}{\max(|\nabla_y Y|)}\end{aligned}\quad (12)$$

Finally, the Weighted Gradient Difference Loss (WGDL) can be expressed as follows:

$$\begin{aligned}\mathcal{L}_{\text{WGDL}}(X, Y) &= \left(\sum_{\substack{i=1 \\ j=1}}^{H,W} W_{\nabla_x}(i, j) \cdot \left| |\nabla_x X_{i,j}| - |\nabla_x Y_{i,j}| \right|^\alpha \right. \\ &\quad \left. + \sum_{\substack{i=1 \\ j=1}}^{H,W} W_{\nabla_y}(i, j) \cdot \left| |\nabla_y X_{i,j}| - |\nabla_y Y_{i,j}| \right|^\alpha \right) / 2\end{aligned}\quad (13)$$

Note that the masked pixels are excluded from the loss.

4. Experiments

4.1. Experimental Setup

4.1.1. Evaluation Metrics

To evaluate the performance of the model, we report four complementary metrics: the coefficient of determination (R^2), the MAE, the root mean squared error (RMSE) and the relative mean absolute error (rMAE). R^2 measures how well the predicted values follow the variability of the true heights, with higher values indicating better explanatory power. MAE reflects the average magnitude of the prediction errors, while RMSE emphasizes larger errors more strongly and, therefore, highlights occasional large deviations. Finally, rMAE expresses the average error relative to the true values, allowing comparison across height ranges with different scales.

4.1.2. Model Configuration

We evaluate THREASURE-NET at three spatial resolutions: 10 m, 5 m, and 2.5 m. Only pixels labeled as vegetation are used for training – specifically, permanent vegetation taller than 1.5 m. A mask is applied to exclude non-vegetation pixels.

All models share the same high-level architecture, which includes an RDB feature extraction block, a temporal transformer for multi-temporal fusion, a super-resolution block, and an MLP prediction head. For the 10 m model, the super-resolution block is omitted, as no upscaling is required. Hyperparameters were chosen based on preliminary experiments and practical constraints associated with the extensive training time, with an additional objective of minimizing prediction error.

The RDB-FE block uses 5 RDB blocks with 5 layers each in the 5 m and 2.5 m models, and 4 dense blocks with 4 layers in the 10 m model. The channel growth rate and output feature dimension are fixed at 24 and 64 across all models. The 10 m model uses a smaller RDB configuration since no super-resolution step is applied, while increasing the RDB size for the 2.5 m model did not yield performance improvements during training.

The temporal transformer employs 4 attention heads and a hidden dimension of 16 to process the multi-temporal inputs. For positional encoding, a scaling constant of $\tau = 365$ is used for both LiDAR and Sentinel-2 acquisition dates.

The super-resolution block applies upscaling factors of $r = 2$ and $r = 4$ for the 5 m and 2.5 m models, respectively, with the convolutional filter size increasing from 64 to 256 for each upscaling step.

Feature sizes F_1 and F_2 are both set to 64. Temporal transformer parameters are set to 4 heads with feature size of 16 for each head.

Finally, the prediction head consists of an MLP with layer sizes (64, 128, 64) that outputs the final single-channel height estimate.

The maximum time-series length is set to 12, and all series shorter than 5 observations are discarded. During training, a random sampling strategy is applied when the time-series length exceeds 12, whereas an equal-range sampling strategy is used during validation to ensure consistency of the validation data.

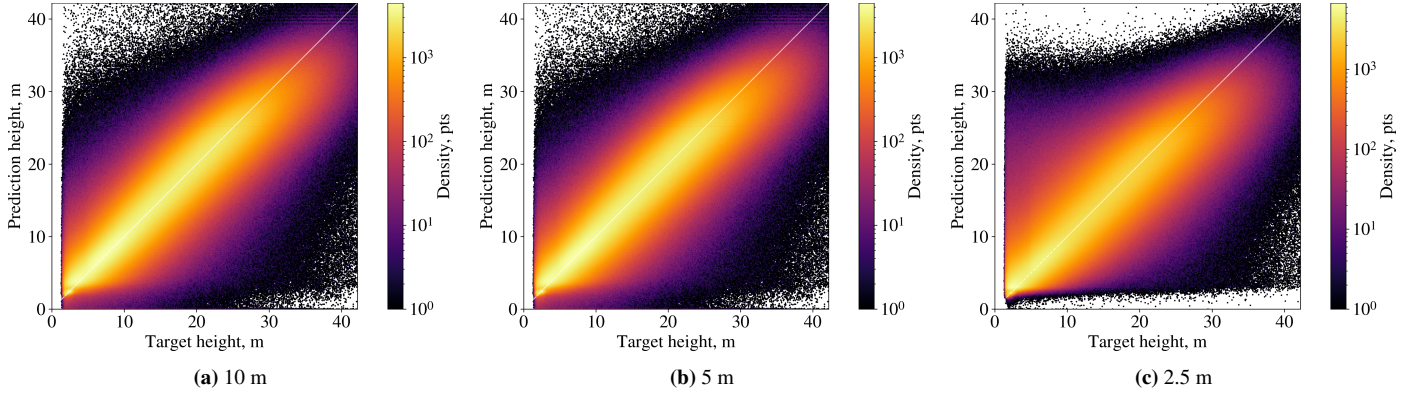


Figure 4: Prediction–target scatterplots for our 10 m, 5 m, and 2.5 m models. For visualization purposes, we randomly sampled an equal number of points (~96 million) from each model, corresponding to the total number of points in the 10 m dataset. The identity line is shown in white. Note that although the minimum target values in the dataset are set to 1.5 m, we report the model predictions without applying any clipping.

Table 1: Quantitative results for our models of 10, 5 and 2.5m resolutions. We also report the performance of two other recent state-of-the-art algorithms: FORMS-T (Schwartz et al., 2025) at 10m and Open-Canopy (Fogel et al., 2025) at 1.5m resolution. N/R stands for “Not Reported”.

Model	Res., m	MAE, m	MAE, %	R2	RMSE, m
THREASURE-Net	10	2.62	22.0	0.75	3.56
	5	2.72	25.4	0.72	3.70
	2.5	2.88	30.0	0.67	3.91
Open-Canopy	1.5	2.52	22.9	N/R	4.02
FORMS-T	10	3.06	N/R	0.68	N/R

The input Sentinel-2 patches contain 64×64 pixels (640×640 m 2), augmented with border margins that are passed through the model but discarded from the output before loss computation and inference, in order to avoid border effects due to 2D convolution operations. During training, we apply a random sampling strategy within the borders of each LiDAR HD patch (1×1 km 2), whereas during validation the central region of the patch is systematically selected. For this reason, the initial Sentinel-2 patches were constructed with 250 m margins on each side relative to the LiDAR patches.

As mentioned in Section 2, MAE and WGDL losses are used for model optimization. All input features were standardized to ensure stable training.

Model training and evaluation were performed on the CNES TREX HPC cluster, equipped with NVIDIA A100 and H100 GPUs. The implementation used PyTorch 2.5.1 with CUDA 11.8. Experiments were executed in mixed-precision mode to improve computational efficiency.

The network was trained using the Adam optimizer with a cosine annealing with warm restarts scheduler (Loshchilov and Hutter, 2016), where the learning rate decays at the beginning of each new cycle by a factor of 0.25 with the initial learning rate set to 10^{-3} . We used a batch size of 32 and accumulated gradients over 4 steps, resulting in an effective batch size of 128.

The training took roughly 3 days for each model.

4.2. Results and Discussion

4.2.1. Quantitative Results

In this subsection, we report the qualitative results of our model performance at different resolutions. The different metrics are reported in Table 1, along with the performance of two other recent state-of-the-art algorithms: FORMS-T and Open-Canopy, taken from the original articles. FORMS-T (Schwartz et al., 2025) uses single-date Sentinel-1 and Sentinel-2 imagery, together with GEDI LiDAR data as reference, to predict canopy structure at 10 m resolution. Open-Canopy (Fogel et al., 2025), in contrast, relies on a single VHR SPOT-6/7 image combined with LiDAR HD to map fine-scale canopy height at 1.5 m.

Although Open-Canopy obtains the lowest MAE overall, its RMSE is higher than the RMSE achieved by THREASURE-Net at each of the three resolutions. This indicates that Open Canopy performs well on average errors but struggles more with extreme values, tending to regress predictions toward the mean. In our case, quantitative performance decreases as the target resolution becomes finer. Nevertheless, the 2.5 m version of our model remains competitive with Open-Canopy, despite relying exclusively on freely available 10 m Sentinel-2 imagery. By contrast, Open-Canopy is trained on 1.5 m SPOT-6/7 data, which are commercial products or accessible only through specific research agreements. This highlights an important advantage of our approach: comparable performance can be achieved without relying on costly high-resolution remote sensing input data. Moreover, all variants of THREASURE-Net reached better results than 10 m resolution FORMS-T, despite relying on Sentinel-2 data only, whereas FORMS-T uses Sentinel-1 and

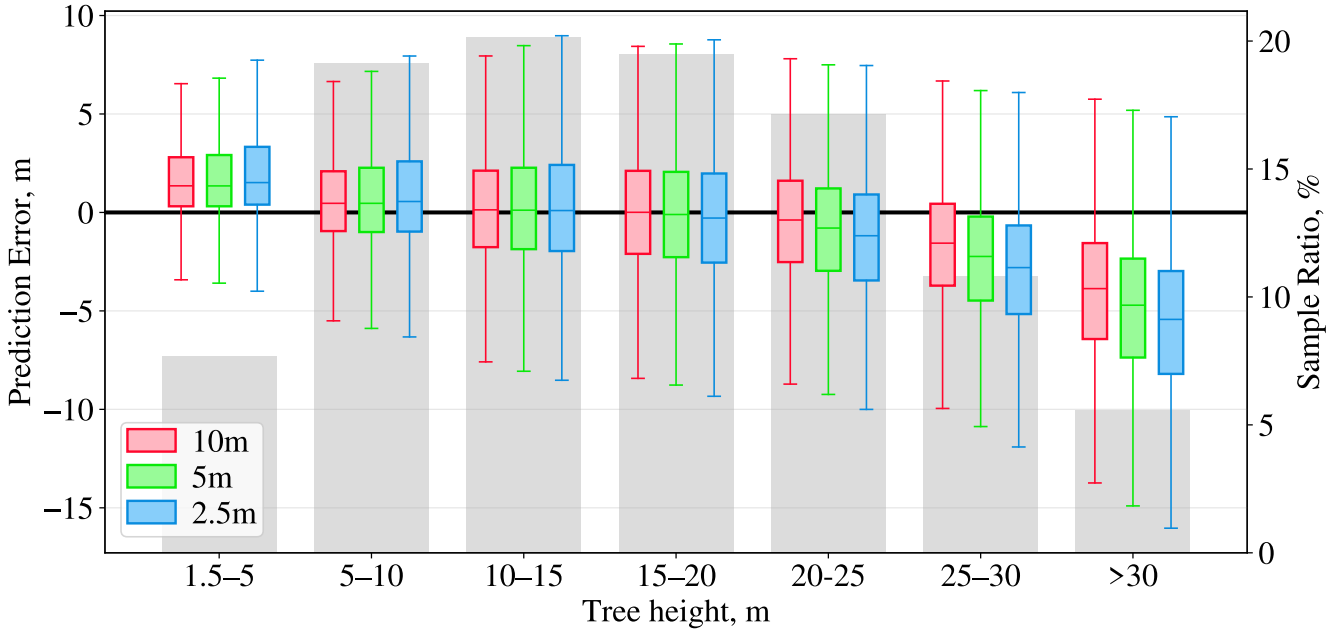


Figure 5: Error distribution across canopy-height bins (1.5–5, 5–10, 10–15, 15–20, 20–25, 25–30, >30 m) for our models at different output resolutions in a form of box-and-whisker plots. A boxplot shows the median and the interquartile range (IQR) (from the 1st to the 3rd quartile), with whiskers extending to the most extreme values within $1.5 \times \text{IQR}$. Gray bars indicate the proportion of samples falling into each bin relative to the entire dataset.

Sentinel-2 data, which requires considerably heavier data processing. Figure 4 presents the prediction–target scatterplots for our models. The 10 m model produces predictions that cluster closely around the identity line, indicating strong agreement with the target values. For the 5 m and 2.5 m models, the point dispersion becomes increasingly noticeable. Interestingly, although the 2.5 m model exhibits the largest overall spread around the identity line, it produces fewer extreme errors than the 10 m and 5 m models. In contrast, the frequency of extreme errors increases as resolution decreases.

Figure 5 shows the error distribution across tree-height bins (1.5–5, 5–10, 10–15, 15–20, 20–25, 25–30, and >30 m) using box-and-whisker plots. Overall, all three resolutions exhibit similar behavior, with a slight degradation in performance for the smallest and tallest trees. In contrast, for mid-range heights (10–15 and 15–20 m), the models perform nearly identically, with median errors close to zero. Moreover, all models tend to overestimate low height values, while for higher values they exhibit the opposite behavior. The most noticeable performance differences between the models occur above 25 m, where their accuracy drops more sharply than in the mid-range bins. This may be explained by the uneven distribution of tree heights in the dataset or by the limitations of Sentinel-2 in distinguishing fine spectral differences in short and tall forest stands — an issue that could be addressed in future work.

4.2.2. Qualitative Results

In this subsection, we qualitatively evaluate the capacity of our algorithm to produce sharp and fine-grained textures at 5

and 2.5 m resolutions. Evaluating super-resolution can be a challenging task, as the evaluation metrics often do not take into account geometric distortions between two datasets (Michel et al., 2025). Moreover, in our case, in the absence of similar algorithms, SR metrics might be difficult to interpret for our results alone. Therefore, we present visual results of our algorithm as well as Frequency Attenuation Profiles (FAP) for the SR task. Moreover, note that the quantitative results of tree height prediction showed in the previous subsection can also be used to qualify the super-resolution task.

Figure 6 illustrates the predictions obtained for a 640×640 m forest patch located in the south-west of France. A progressive gain in spatial detail can be observed when moving from the 10 m prediction (Subfigure 6b) to the 5 m (Subfigure 6c) and finally to the 2.5 m prediction (Subfigure 6d). For comparison, we additionally provide bicubic upsampling of the 10 m and 5 m models outputs to 5 m (Subfigure 6g) and 2.5 m (Subfigure 6h), respectively. This allows us to highlight the benefit of deep-learning-based super-resolution compared with a classical interpolation method.

Although the super-resolved predictions do not reach the full level of detail present in the reference image, it is nevertheless possible to distinguish tree crown shapes and fine-scale structures such as forest gaps. The improvement from 10 m to 5 m resolution is particularly noticeable, whereas the enhancement from 5 m to 2.5 m is more subtle. When comparing the bicubic 5 → 2.5 m upsampling with the 2.5 m super-resolved output, small gaps appear sharper in the latter, but it introduces little new structural information. This behavior is consistent with the

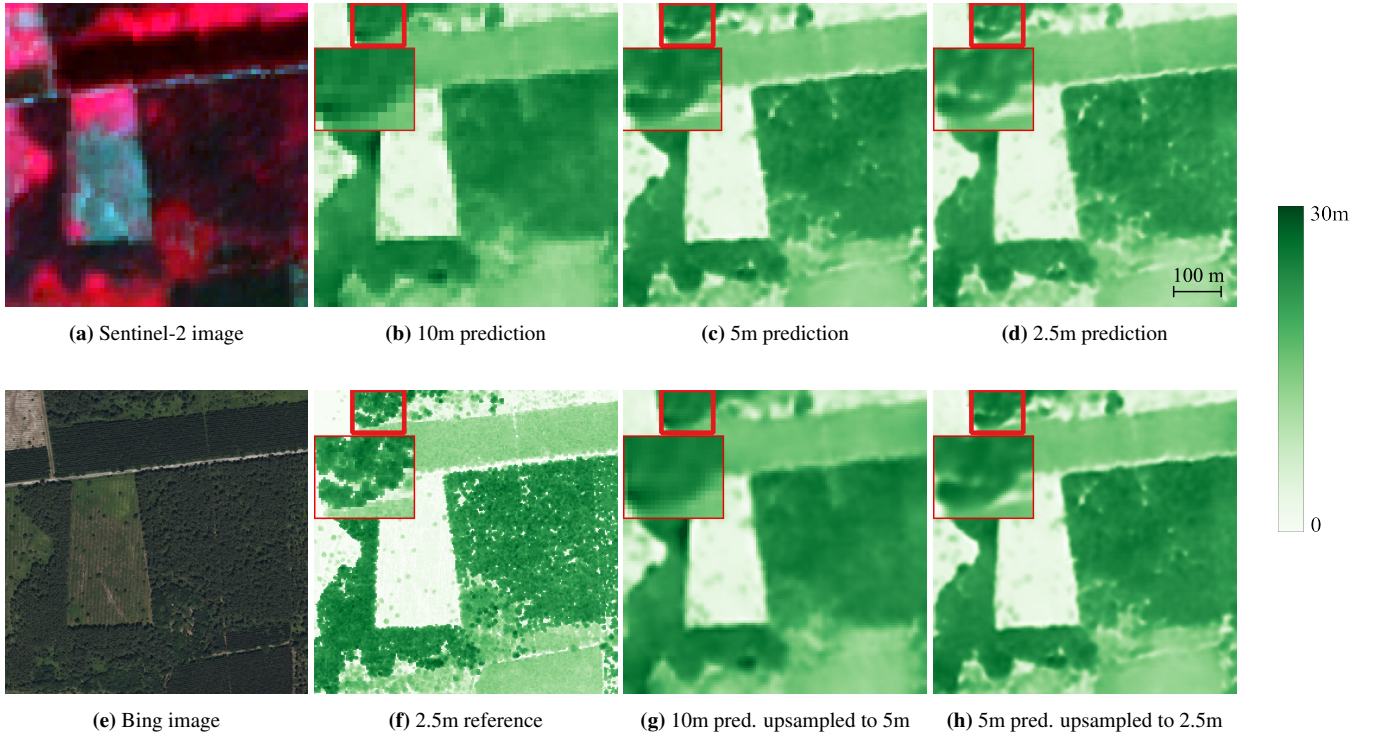


Figure 6: 640×640 m Tree height prediction patches centred on 44.893°N and 0.997°W . Subfigures (b)–(d) present the prediction results of our model at 10 m, 5 m, and 2.5 m resolutions, respectively. Subfigure (a) shows a Sentinel-2 image from the input time series acquired on 7 July 2023, while (f) depicts the reference LiDAR-derived height map at 2.5 m resolution. Subfigures (g) and (h) display the 10 and 5 m predictions upsampled to 5 m and 2.5 m respectively using bicubic interpolation. Finally, (e) provides a VHR Bing image for visual comparison. Zoomed-in views (top-left corner) highlight differences in fine details between predictions. No masking is applied in these examples.

limited amount of spatial information available in Sentinel-2 imagery, which constrains the degree of recoverable fine-scale detail.

To evaluate the quality of super-resolution (SR) frequency restoration, we use the Frequency Attenuation Profile (FAP) metric based on Discrete Fourier Transform (DFT) (Michel et al., 2025), as it is not sensitive to cross-dataset distortions and provides a robust frequency-domain comparison. FAP indicates how strongly each spatial frequency component is preserved or attenuated in an image. Low frequencies correspond to large-scale structures, whereas high frequencies capture fine textures and edges. By comparing the attenuation curves of the HR reference, the SR prediction, and the lower resolution input upsampled with bicubic interpolation, we can assess how effectively the model restores or preserves spatial details.

Figure 7 presents the normalized log-Frequency Attenuation Profiles for the 5 m and 2.5 m SR predictions, the corresponding HR reference data, and the 10 m and 5 m THREASURE-Net predictions upsampled to 5 m and 2.5 m, respectively, using bicubic interpolation. The results are presented for the same patch as in Figure 6. For both resolutions, SR predictions exhibit a progressive attenuation as frequency increases, reflecting the loss or smoothing of fine spatial details relative to the HR reference, with stronger degradation at 2.5 m. At 5 m, the SR model consistently outperforms bicubic upsampling across most of the frequency spectrum. At 2.5 m, although improvements over bicubic interpolation are modest in the mid-

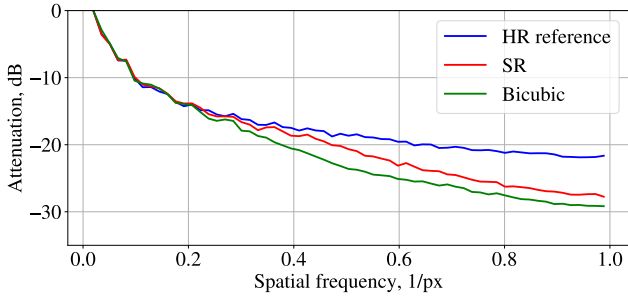
frequency range, the SR output still shows a clear advantage at higher frequencies.

4.2.3. Temporal monitoring

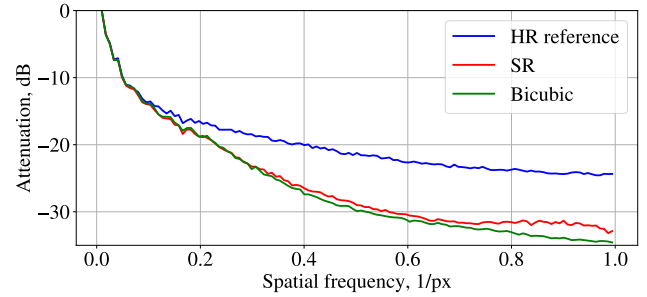
Figure 8 illustrates fine-scale change detection in the Chantilly forest. Although our model was not explicitly trained to predict non-vegetation areas – assigning them a default height of zero – it still produces values close to zero in these regions, making change detection feasible. Despite this constraint, the loss of vegetation is clearly captured, particularly at the 2.5 m and 5 m resolution. The reference VHR SPOT images from 2022 and 2023, as well as the ALS-derived height change map at 1.5 m resolution (between February 2022 and September 2023), are taken from the Open-Canopy repository (Fogel et al., 2025).

Figure 9 illustrates the regrowth profile of *Pinus pinaster* in the Landes of Gascogne. In this region, sanitary clear-cuts are regularly performed, followed by the planting of young trees, making the monitoring of early-stage growth particularly important. We delimitate a forest parcel with young pine trees to follow its regrowth profile.

The plot shows the median tree height per parcel, accompanied by the 25th and 75th percentiles of parcel-level height values. The 2.5 m and 5 m predictions exhibit very similar behaviour across all ages. In contrast, the 10 m model reports higher height values for young stands. This discrepancy is not necessarily an error: at finer resolutions (2.5 m and 5 m), young



(a) 5 m



(b) 2.5 m

Figure 7: Normalized log-Frequency Attenuation Profile FAP for HR reference patch, SR results and bicubic interpolation for 5 m (a) and 2.5 m (b) predictions for patch presented in Figure 6. Bicubic interpolation profiles correspond to Subfigures 6g and 6h respectively. To maintain consistency, we used HR reference data with the same native resolution for both predictions. Spatial frequencies in x axis correspond to normalized spatial frequencies $f = \frac{f_n}{f_N}$, where f_N is the maximum spatial frequency that can be represented at a given image resolution.

trees are sparsely distributed and gaps between them are visible, whereas at 10 m these gaps disappear at 10 m resolution, since the model uses the 95th percentile of point heights within each pixel, yielding higher height estimates. As stands grow older, this difference gradually diminishes. The similarity between the 2.5 m and 5 m curves for young stands suggests that the 2.5 m model captures only limited additional structural detail compared to the 5 m model.

Although the predicted growth curve shows occasional small drops, the overall tendency remains within the expected error range. These slight decreases may reflect periods of drought or other meteorological events that affect the spectral response of the vegetation, leading to temporarily lower predicted heights.

Finally, the predicted regrowth curve aligns with the expected growth dynamics of young *Pinus pinaster* in the Landes forest (Chevalier et al., 2024), which reaches approximately 1 m per year, depending on the climatic conditions. This confirms that our method is well suited for monitoring early-stage forest regrowth.

Moreover, we evaluated the effectiveness of temporal conditioning by explicitly generating predictions at different dates throughout the year. Although no reference data are available at a monthly frequency, the expected seasonal growth pattern can still be observed when comparing predictions across the specified dates.

5. Conclusion

In this paper, we have introduced THREASURE-Net, a novel end-to-end framework for super-resolved tree canopy height estimation. Our approach generates high-resolution annual predictions at 2.5 m and 5 m directly from Sentinel-2 time series with 10 m resolution, supervised with LiDAR HD-derived canopy height data. THREASURE-Net outperforms existing Sentinel-2-based methods for forest height prediction and achieves performances comparable to approaches relying on 1.5 m SPOT-6/7 imagery. Our model achieves mean absolute errors of 2.62 m, 2.72 m, and 2.88 m at 2.5 m, 5 m, and 10 m

resolution, respectively, and can be used for change detection and tree growth monitoring.

Future work will focus on mitigating the imbalance across canopy height classes and improving the prediction of very small and very tall trees. Incorporating radar data could be a promising direction, as it provides complementary structural information.

Finally, we plan to integrate a tree/non-tree classification module, enabling a fully end-to-end system that does not rely on an external forest mask.

Acknowledgements

Ekaterina Kalinicheva, Florian Mouret and Milena Planells were supported by the PC ALAMOD from the PEPR Fair-Carbon. Florian Helen and Stéphane Mermoz were supported by a “R&T: Estimation annuelle de paramètres biogéophysiques des forêts françaises et leurs changements par IA” grant from the Centre National d’Études Spatiales (CNES) (Marché n°5700013599).

We would like to express our sincere gratitude to Julien Michel and Jordi Inglada for their assistance and valuable advice on deep learning methods, without which this work would not have been possible.

References

- Abadal, S., Salgueiro, L., Marcello, J., Vilaplana, V., 2021. A dual network for super-resolution and semantic segmentation of sentinel-2 imagery. *Remote Sensing* 13. URL: <https://www.mdpi.com/2072-4292/13/22/4547>, doi:10.3390/rs13224547.
- Ahmed, O.S., Franklin, S.E., Wulder, M.A., White, J.C., 2015. Characterizing stand-level forest canopy cover and height using landsat time series, samples of airborne lidar, and the random forest algorithm. *ISPRS Journal of Photogrammetry and Remote Sensing* 101, 89–101. URL: <https://www.sciencedirect.com/science/article/pii/S0378-389015000117>

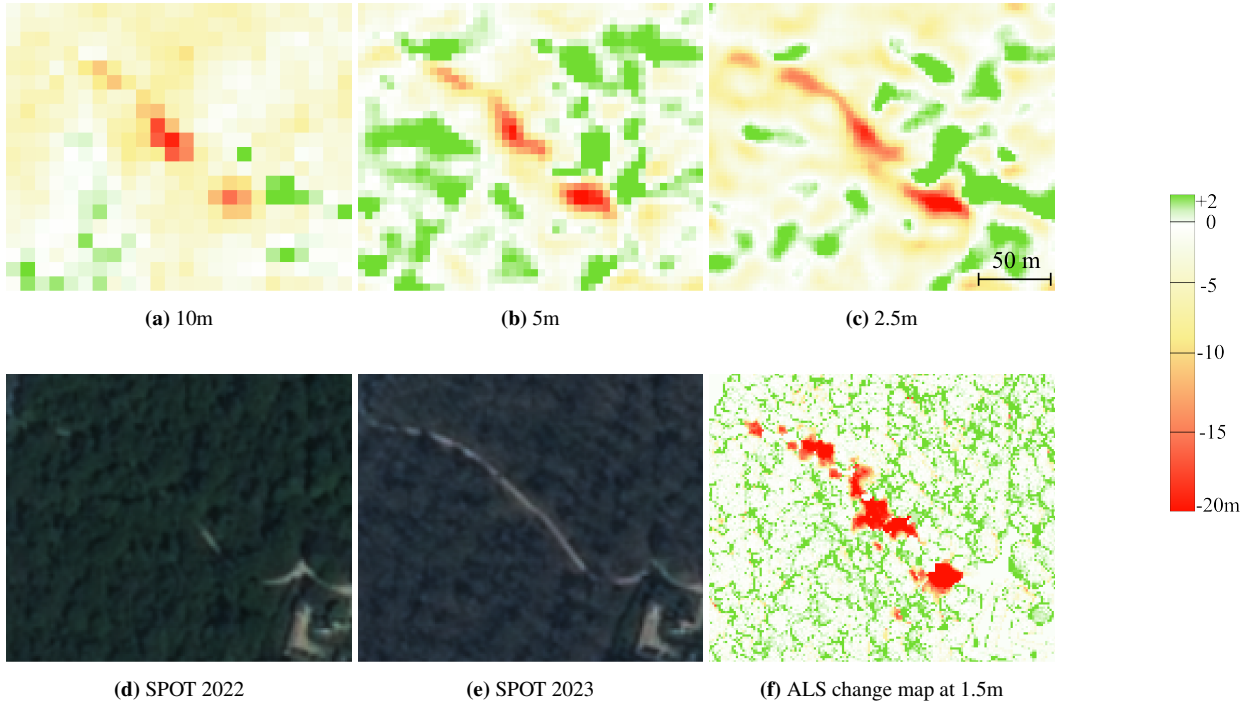


Figure 8: Change detection example centered on 49.187°N and 2.573°E. Subfigures (a)–(c) present the prediction results of our model at 10 m, 5 m, and 2.5 m resolutions, respectively. Subfigure (d) and (e) show reference VHR SPOT images acquired corresponding to 2022 and 2023 acquisition years, while (f) depicts the reference ALS-derived height change map between September 2023 and February 2022 at 1.5 m resolution. Both SPOT and ALS images are taken from Open-Canopy repository (Fogel et al., 2025).

article/pii/S0924271614002755, doi:<https://doi.org/10.1016/j.isprsjprs.2014.11.007>.

Aitken, A., Ledig, C., Theis, L., Caballero, J., Wang, Z., Shi, W., 2017. Checkerboard artifact free sub-pixel convolution: A note on sub-pixel convolution, resize convolution and convolution resize. URL: <https://arxiv.org/abs/1707.02937>, arXiv:1707.02937.

Besic, N., Picard, N., Vega, C., Bontemps, J.D., Hertzog, L., Renaud, J.P., Fogel, F., Schwartz, M., Pellissier-Tanon, A., Destouet, G., Mortier, F., Planells-Rodriguez, M., Ciais, P., 2025. Remote-sensing-based forest canopy height mapping: some models are useful, but might they provide us with even more insights when combined? Geoscientific Model Development 18, 337–359. doi:10.5194/gmd-18-337-2025.

Bugmann, H., Seidl, R., 2022. The evolution, complexity and diversity of models of long-term forest dynamics. Journal of Ecology 110, 2288–2307. URL: <https://besjournals.onlinelibrary.wiley.com/doi/abs/10.1111/1365-2745.13989>, doi:<https://doi.org/10.1111/1365-2745.13989>.

Cally, J.G., et al., 2025. Declining trends in canopy disturbance across reserve forest landscapes of the northeastern us. Forest Ecology and Management 578, 122465. doi:10.1016/j.foreco.2024.122465.

Cao, Y., Weng, Q., 2024. A deep learning-based super-resolution method for building height estimation at 2.5 m spatial resolution in the northern hemisphere. Remote Sensing of Environment 310, 114241. URL: <https://www.sciencedirect.com/science/article/pii/S0034425724002591>, doi:<https://doi.org/10.1016/j.rse.2024.114241>.

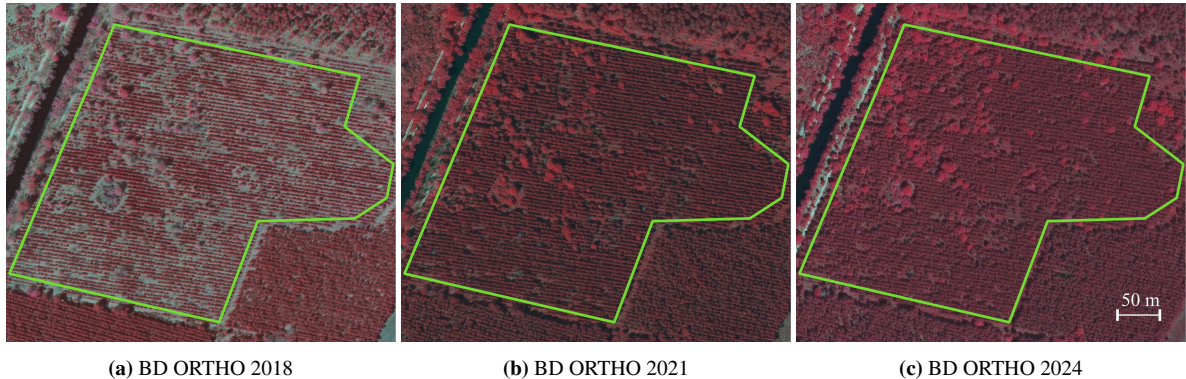
Chevalier, R., Catapano, A., Pommier, R., Montemurro, M., 2024. A review on properties and variability of *pinus pinaster* ait. ssp. *atlantica* existing in the landes of gascogne. Journal of Wood Science 70. doi:10.1186/s10086-024-02127-3.

Coops, N.C., Tompalski, P., Goodbody, T.R., Queinnec, M., Luther, J.E., Bolton, D.K., White, J.C., Wulder, M.A., van Lier, O.R., Hermosilla, T., 2021. Modelling lidar-derived estimates of forest attributes over space and time: A review of approaches and future trends. Remote Sensing of Environment 260, 112477. URL: <https://www.sciencedirect.com/science/article/pii/S0034425721001954>, doi:<https://doi.org/10.1016/j.rse.2021.112477>.

Cresson, R., 2022. Sr4rs: A tool for super resolution of remote sensing images. Journal of Open Research Software 10.

Deng, J., Hong, D., Li, C., Yokoya, N., 2025. Joint super-resolution and segmentation for 1-m impervious surface area mapping in china's yangtze river economic belt. URL: <https://arxiv.org/abs/2505.05367>, arXiv:2505.05367.

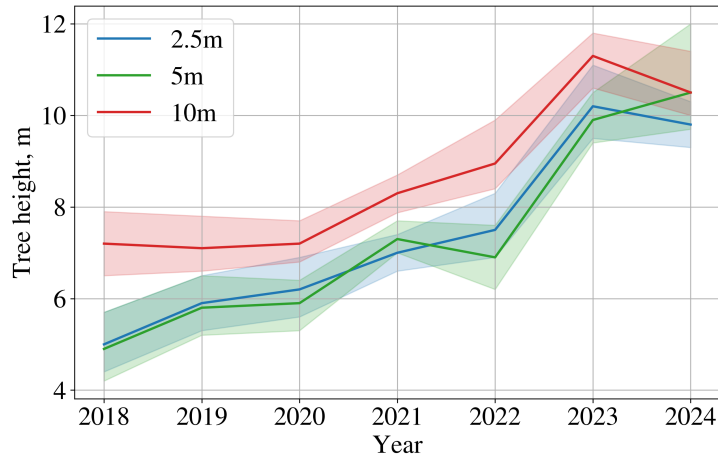
Deudon, M., Kalaitzis, A., Goytom, I., Arefin, M.R., Lin, Z., Sankaran, K., Michalski, V., Kahou, S.E., Cornebise, J., 2024. A deep learning-based super-resolution method for building height estimation at 2.5 m spatial resolution in the northern hemisphere. Remote Sensing of Environment 310, 114241. URL: <https://www.sciencedirect.com/science/article/pii/S0034425724002591>, doi:<https://doi.org/10.1016/j.rse.2024.114241>.



(a) BD ORTHO 2018

(b) BD ORTHO 2021

(c) BD ORTHO 2024



(d) *Pinus Pinaster* regrowth profile.

Figure 9: Regrowth monitoring of *Pinus Pinaster* example centered on 44.894°N and 1.13°W. Subfigures (a)–(c) present the BD ORTHO images for 2018, 2021 and 2024 year. Subfigure (d) shows the regrowth profile for our model at 10 m, 5 m, and 2.5 m resolutions. The thick line corresponds to a median value within the delineated parcel, with the margins extending to 25th and 75th percentiles.

J., Bengio, Y., 2020. Highres-net: Recursive fusion for multi-frame super-resolution of satellite imagery. CoRR abs/2002.06460. URL: <https://arxiv.org/abs/2002.06460>, arXiv:2002.06460.

Drusch, M., Del Bello, U., Carlier, S., Colin, O., Fernandez, V., Gascon, F., Hoersch, B., Isola, C., Labinti, P., Martimort, P., Meygret, A., Spoto, F., Sy, O., Marchese, F., Bargellini, P., 2012. Sentinel-2: Esa's optical high-resolution mission for gmes operational services. *Remote Sensing of Environment* 120, 25–36. URL: <https://www.sciencedirect.com/science/article/pii/S0034425712000636>, doi:<https://doi.org/10.1016/j.rse.2011.11.026>. the Sentinel Missions - New Opportunities for Science.

Dubayah, R., Blair, J.B., Goetz, S., Fatooyinbo, L., Hansen, M., Healey, S., Hofton, M., Hurt, G., Kellner, J., Luthcke, S., Armston, J., Tang, H., Duncanson, L., Hancock, S., Jantz, P., Marselis, S., Patterson, P.L., Qi, W., Silva, C., 2020. The global ecosystem dynamics investigation: High-resolution laser ranging of the earth's

forests and topography. *Science of Remote Sensing* 1, 100002. URL: <https://www.sciencedirect.com/science/article/pii/S2666017220300018>, doi:<https://doi.org/10.1016/j.srs.2020.100002>.

Duncanson, L., Hunka, N., Jucker, T., Armston, J., Harris, N., Fatooyinbo, L., Williams, C.A., Atkins, J.W., Raczka, B., Serbin, S., Keller, M., Dubayah, R., Babcock, C., Cochrane, M.A., Hudak, A., Hurt, G.C., Montesano, P.M., Moskal, L.M., Park, T., Saatchi, S., Silva, C.A., Tang, H., Vargas, R., Weiskittel, A., Wessels, K., Goetz, S.J., 2025. Spatial resolution for forest carbon maps. *Science* 387, 370–371. doi:[10.1126/science.adt6811](https://doi.org/10.1126/science.adt6811).

FAO, 2025. Global Forest Resources Assessment 2025. Food and Agriculture Organization of the United Nations, Rome. URL: <https://openknowledge.fao.org/server/api/core/bitstreams/12322cae-5b20-4be2-927a-72a86fd319e9/content>.

Fassnacht, F.E., White, J.C., Wulder, M.A., Næsset, E., 2023. Remote sensing in forestry: current challenges,

considerations and directions. *Forestry: An International Journal of Forest Research* 97, 11–37. URL: <https://doi.org/10.1093/forestry/cpad024>, doi:10.1093/forestry/cpad024.

Fogel, F., Perron, Y., Besic, N., Saint-André, L., Pellissier-Tanon, A., Schwartz, M., Boudras, T., Fayad, I., d'Aspremont, A., Landrieu, L., Ciais, P., 2025. Open-canopy: Towards very high resolution forest monitoring, in: 2025 IEEE/CVF Conference on Computer Vision and Pattern Recognition (CVPR), pp. 1395–1406. doi:10.1109/CVPR52734.2025.00138.

Garnot, V.S.F., Landrieu, L., 2020. Lightweight temporal self-attention for classifying satellite image time series. CoRR abs/2007.00586. URL: <https://arxiv.org/abs/2007.00586>, arXiv:2007.00586.

He, K., Zhang, X., Ren, S., Sun, J., 2015. Deep residual learning for image recognition. CoRR abs/1512.03385. URL: <http://arxiv.org/abs/1512.03385>, arXiv:1512.03385.

Lang, N., Jetz, W., Schindler, K., Wegner, J.D., 2023. A high-resolution canopy height model of the earth. *Nature Ecology & Evolution* 7, 1778–1789.

Lei, S., Shi, Z., Wu, X., Pan, B., Xu, X., Hao, H., 2019. Simultaneous super-resolution and segmentation for remote sensing images. *IGARSS 2019 - 2019 IEEE International Geoscience and Remote Sensing Symposium*, 3121–3124URL: <https://api.semanticscholar.org/CorpusID:208037945>.

Lepcha, D.C., Goyal, B., Dogra, A., Goyal, V., 2023. Image super-resolution: A comprehensive review, recent trends, challenges and applications. *Information Fusion* 91, 230–260. URL: <https://www.sciencedirect.com/science/article/pii/S1566253522001762>, doi:<https://doi.org/10.1016/j.inffus.2022.10.007>.

Liu, D., Zhong, L., Wu, H., Li, S., Li, Y., 2025. Remote sensing image super-resolution reconstruction by fusing multi-scale receptive fields and hybrid transformer. *Scientific Reports* 15. doi:10.1038/s41598-025-86446-5.

Liu, Y., Kumar, M., Katul, G.G., Porporato, A., 2019. Reduced resilience as an early warning signal of forest mortality. *Nature Climate Change* 9, 880–885. URL: <https://doi.org/10.1038/s41558-019-0583-9>, doi:10.1038/s41558-019-0583-9.

Loshchilov, I., Hutter, F., 2016. Sgdr: Stochastic gradient descent with warm restarts. doi:10.48550/arXiv.1608.03983.

Luo, Z., Song, B., Shen, L., 2024. Satdiffmoe: A mixture of estimation method for satellite image super-resolution with latent diffusion models. CoRR abs/2406.10225. URL: <https://doi.org/10.48550/arXiv.2406.10225>, doi:10.48550/ARXIV.2406.10225, arXiv:2406.10225.

Mermoz, S., Prieto, J.D., Planells, M., Morin, D., Koleck, T., Mouret, F., Bouvet, A., Le Toan, T., Sheeren, D., Hamrouni, Y., et al., 2024. Sub-monthly assessment of temperate forest clear-cuts in mainland france. *IEEE Journal of Selected Topics in Applied Earth Observations and Remote Sensing*.

Michel, J., Kalinicheva, E., Inglada, J., 2025. Revisiting remote sensing cross-sensor single image super-resolution: The overlooked impact of geometric and radiometric distortion. *IEEE Transactions on Geoscience and Remote Sensing* 63, 1–22. doi:10.1109/TGRS.2025.3572548.

Mitchell, A., Rosenqvist, A., Mora, B., 2017. Current remote sensing approaches to monitoring forest degradation in support of countries measurement, reporting and verification (mrv) systems for redd+. *Carbon Balance and Management* 12, 9. doi:10.1186/s13021-017-0078-9.

Morin, D., Planells, M., Mermoz, S., Mouret, F., 2023. Estimation of forest height and biomass from open-access multi-sensor satellite imagery and gedi lidar data: high-resolution maps of metropolitan france. arXiv preprint arXiv:2310.14662.

Müller, M., Ekhtiari, N., Almeida, R., Rieke, C., 2020. Super-resolution of multispectral satellite images using convolutional neural networks. *ISPRS Annals of Photogrammetry, Remote Sensing and Spatial Information Sciences* V-1-2020, 33–40. doi:10.5194/isprs-annals-V-1-2020-33-2020.

Nie, D., Trullo, R., Lian, J., Wang, L., Petitjean, C., Ruan, S., Wang, Q., Shen, D., 2018. Medical image synthesis with deep convolutional adversarial networks. *IEEE Transactions on Biomedical Engineering* 65, 2720–2730. doi:10.1109/TBME.2018.2814538.

Okabayashi, A., Audebert, N., Donike, S., Pelletier, C., 2024. Cross-sensor super-resolution of irregularly sampled sentinel-2 time series, pp. 502–511. doi:10.1109/CVPRW63382.2024.00055.

Pelletier, C., Webb, G.I., Petitjean, F., 2018. Temporal convolutional neural network for the classification of satellite image time series. CoRR abs/1811.10166. URL: <http://arxiv.org/abs/1811.10166>, arXiv:1811.10166.

Salgueiro Romero, L., Marcello, J., Vilaplana, V., 2022. Segesrgan: A multi-task network for super-resolution and semantic segmentation of remote sensing images. *Remote Sensing* 14, 5862. doi:10.3390/rs14225862.

Santoro, M., Cartus, O., Quegan, S., Kay, H., Lucas, R.M., Araza, A., Herold, M., Labrière, N., Chave, J., Rosenqvist, Å., et al., 2024. Design and performance of the climate change initiative biomass global retrieval algorithm. *Science of remote sensing* 10, 100169.

Schwartz, M., Ciais, P., Sean, E., de Truchis, A., Vega, C., Besic, N., Fayad, I., Wigneron, J.P., Brood, S., Pelissier-Tanon, A., Pauls, J., Belouze, G., Xu, Y., 2025. Retrieving yearly forest growth from satellite data: A deep learning based approach. *Remote Sensing of Environment* 330, 114959. URL: <https://www.sciencedirect.com/science/article/pii/S0034425725003633>, doi:<https://doi.org/10.1016/j.rse.2025.114959>.

Shi, W., Caballero, J., Huszár, F., Totz, J., Aitken, A.P., Bishop, R., Rueckert, D., Wang, Z., 2016. Real-time single image and video super-resolution using an efficient sub-pixel convolutional neural network, in: 2016 IEEE Conference on Computer Vision and Pattern Recognition (CVPR), pp. 1874–1883. doi:[10.1109/CVPR.2016.207](https://doi.org/10.1109/CVPR.2016.207).

Simard, M., Pinto, N., Fisher, J.B., Baccini, A., 2011. Mapping forest canopy height globally with spaceborne lidar. *Journal of Geophysical Research: Biogeosciences* 116.

Vu-Duc, A., Nguyen-Vi, K., Bui-Quoc, B., Kamel, N., 2025. A comprehensive survey of super-resolution remote sensing image datasets: Evolution, challenges, and future directions. *IEEE Access* 13, 145350–145372. doi:[10.1109/ACCESS.2025.3599535](https://doi.org/10.1109/ACCESS.2025.3599535).

Wang, P., Bayram, B., Sertel, E., 2022a. A comprehensive review on deep learning based remote sensing image super-resolution methods. *Earth-Science Reviews* 232, 104110. URL: <https://www.sciencedirect.com/science/article/pii/S0012825222001945>, doi:<https://doi.org/10.1016/j.earscirev.2022.104110>.

Wang, X., Yi, J., Guo, J., Song, Y., Lyu, J., Xu, J., Yan, W., Zhao, J., Cai, Q., Min, H., 2022b. A review of image super-resolution approaches based on deep learning and applications in remote sensing. *Remote Sensing* 14. URL: <https://www.mdpi.com/2072-4292/14/21/5423>, doi:[10.3390/rs14215423](https://doi.org/10.3390/rs14215423).

Wang, X., Yu, K., Wu, S., Gu, J., Liu, Y., Dong, C., Loy, C.C., Qiao, Y., Tang, X., 2018. ESRGAN: enhanced super-resolution generative adversarial networks. *CoRR* abs/1809.00219. URL: <http://arxiv.org/abs/1809.00219>, arXiv:1809.00219.

Wang, Y., Li, G., Ding, J., Guo, Z., Tang, S., Wang, C., Huang, Q., Liu, R., Chen, J.M., 2016. A combined glas and modis estimation of the global distribution of mean forest canopy height. *Remote Sensing of Environment* 174, 24–43. URL: <https://www.sciencedirect.com/science/article/pii/S0034425715302261>, doi:<https://doi.org/10.1016/j.rse.2015.12.005>.

Wang, Z., Chen, J., Hoi, S.C.H., 2021. Deep learning for image super-resolution: A survey. *IEEE Transactions on Pattern Analysis and Machine Intelligence* 43, 3365–3387. doi:[10.1109/TPAMI.2020.2982166](https://doi.org/10.1109/TPAMI.2020.2982166).

Zhang, Y., Tian, Y., Kong, Y., Zhong, B., Fu, Y., 2018. Residual dense network for image super-resolution. *CoRR* abs/1802.08797. URL: <http://arxiv.org/abs/1802.08797>, arXiv:1802.08797.